Adaptation to Venting Disturbances for Onboard Navigation*

Rachel Mamich † and Renato Zanetti‡
The University of Texas at Austin, Austin, TX, 78712

I. Introduction

In recent years there has been a growing interest in human spaceflight to distant celestial bodies. The Artemis missions are underway and aim to take humans back to the moon for the first time since the Apollo missions in the 1970s. Companies like SpaceX and Blue Origin have expressed an interest in taking humans to Mars. Crewed missions add considerable complexities to spacecraft design and affect many subsystems, including onboard navigation.

An aspect of human spaceflight that has recently received considerable attention is the venting disturbances produced by the Environmental Control & Life Support System (ECLSS), and in particular how to model them and their effect on the navigation and orbit determination solutions [1–4]. Early analysis of crewed Artemis missions modeled venting disturbances as spherical process noise with zero mean [1, 2]. In Joshi et al. [3, 4], it is shown that large discrepancies arise between the nominal trajectory with and without accounting for venting in both direction and magnitude. These findings suggest the need to accurately model the effects of venting perturbations for future crewed missions.

For use onboard spacecraft, dynamics models must be truncated to keep the overall computational demands tractable. Unmodeled dynamics are typically compensated with adjustments to the assumed level of process noise added to the system, typically via extensive testing against a high fidelity model to tune the expected level of noise or 'mismatch'. Joshi et al. have shown crewed Artemis missions must account for perturbations caused by the presence of the crew and the ECLSS system.

The Kalman Filter (KF)[5, 6] operates under the assumption that models of the dynamics and measurements (including the statistics of noises entering the system) are known exactly. In practical aerospace systems, perfect knowledge of the models is not possible; additionally, unexpected events can alter the dynamics of the state or the way that a sensor is functioning. When models become mismatched, it can lead to degraded estimation performance and even filter divergence. The Artemis I mission was not crewed and thus the effects of the ECLSS system have not yet been observed in space. If the actual venting perturbations differ substantially from the models, the overall filter performance will suffer.

Adaptive estimation (or filtering) aims to estimate the state of the system while simultaneously reducing uncertainty in the model [7, 8]. Adaptive filters can be broadly categorized as: correlation methods [7, 9–15], covariance matching

*This work is an extension of the work titled Applying Correlation Methods to Relative Navigation, Paper 2024-377 at the AIAA/AAS Astrodynamics Specialist Conference, Broomfield, CO August 11–15, 2024.

†NSTGRO Fellow and Graduate Student, Aerospace Engineering and Engineering Mechanics, UT Austin, Corresponding Author, rachel.mamich@gmail.com

‡Associate Professor, Aerospace Engineering and Engineering Mechanics, UT Austin.

methods [16–20], maximum likelihood methods [21–23], Bayesian methods [24–26], subspace methods [27], and predictor error methods [28]. In this work, correlation methods are applied to a relative navigation algorithm to enable autonomous, onboard process noise adaptation in the presence of venting perturbations on the target vehicle. This algorithm is referred to as MILTON (Measurement Innovation Leveraging To Obtain Noise). The intent of this paper is to demonstrate the viability of using MILTON to estimate venting disturbances that have direction and a nonzero mean magnitude with an unknown level of uncertainty where the filter begins with no information on the vent directions, magnitudes, or times they will occur. The contributions of this work are:

- An adaptive navigation solution to rendezvous a target vehicle subject to unmodeled vents.
- A novel guarantee of positive definiteness of the adapted process noise covariance matrix by leveraging the known relationships between position, velocity, and acceleration.
- An information formulation of covariance adaptation law to reduce the computational cost.

This paper is organized as follows: Section II, presents background on previous work. Section III, covers the design of the navigation filter. Numeric simulations and results covered in Sections IV.A and IV.B. Section V concludes the major takeaways from this work.

II. Background: Noise Compensation Methods

One of the most popular estimation algorithms in the aerospace industry is the Extended Kalman Filter (EKF). The EKF the dynamics of the system is known modulo white noise with known statistics. In practice, the process noise is selected to bound the uncertainty in the model in order to ensure that the resulting state estimate from the filter does not diverge.

A commonly utilized yet straightforward approach to addressing unmodeled dynamics is State Noise Compensation (SNC) [29]. This method, largely heuristic, requires extensive tuning to achieve reliable usage. Moreover, SNC operates under the assumption that errors are not temporally correlated. Another method for compensating for unknowns in a system is to model the unknown forces using Dynamic Model Compensation (DMC) [29]. DMC allows for time correlation of the errors and it typically models the unknown accelerations as a first or second order Gauss-Markov process. DMC generally outperforms SNC in accuracy of estimate.

Another method of noise compensation is to incorporate consider parameters. Consider parameters are typically used when certain states are not 'totally' observable, but the uncertainty in those states should not be neglected from the uncertainty in the system [29]. In Stauch and Jah consider parameters are employed to add uncertainty to the dynamics model through a spacecraft's ballistic coefficient without needing to update the estimate of the ballistic coefficient [30]. In McCabe and DeMars consider parameters are combined with square root filtering and applied to a ballistic reentry simulation [31].

Fixed noise compensation techniques have significant heritage in the aerospace industry. They all require a priori

information and testing to be set appropriately. A common practice is to estimate the level of process noise for a system by running simulations using the filter dynamics model and comparing the results against a high fidelity model [32], the so-called 'truth' model. While both of these techniques are effective for nominal flight conditions, there have been cases where the noise parameters must be adjusted during the course of a mission [33, 34]. Joshi et al. show that using spherical, white noise uncertainty to compensate for venting associated with the Orion crewed vehicle leads to divergence from the planned nominal trajectory for the Artemis II mission [3, 4]. When the performance differs too far from the expected nominal, the ground must calculate updates and send them to the spacecraft [33, 34].

Including onboard noise adaptation would allow a spacecraft to autonomously adjust to unmodeled perturbations without ground intervention. In Stacey and D'Amico's work, covariance matching is used to allow the SNC and DMC noise models to autonomously adjust the noise levels in the dynamics of spacecraft orbiting an asteroid [19]. This work shows empirically reliable estimates of unmodeled noise in a dual spacecraft system. In Giraldo-Grueso et al. maximum likelihood methods are combined with neural networks to adaptively estimate the atmospheric density that a spacecraft is flying through [35, 36].

III. Navigation Design

This section covers the design of the adaptive relative navigation filter, MILTON. The state space is comprised of the relative inertial target position and velocity, the target vehicle's unmodeled acceleration in the inertial frame, the inertial chaser position and velocity, and accelerometer bias terms in the body frame for the chaser vehicle. The state space is,

$$\mathbf{x} = \begin{bmatrix} (\mathbf{r}_{t/c}^{N})^T & (\mathbf{v}_{t/c}^{N})^T & (\mathbf{a}_{t}^{N})^T & (\mathbf{r}_{c}^{N})^T & (\mathbf{v}_{c}^{N})^T & (\mathbf{b}_{c}^{B_c})^T \end{bmatrix}^T, \tag{1}$$

where $\mathbf{r}$ indicates a position vector, $\mathbf{v}$ indicates a velocity vector, $\mathbf{a}$ indicates an acceleration vector, and $\mathbf{b}$ represents an accelerometer bias vector. In this work, the superscript ^{N} indicates that the vector is represented in the inertial frame and the superscripts ^{B_t} and ^{B_c} indicate that the vectors are represented in the target body frame and the chaser body frame respectively. Lastly, when a vector has a subscript of the form $_{t/c}$ it indicates that the vector is from the chaser to the target vehicle and when the subscript is a single letter like $_{c}$ it indicates that the origin of the vector is the origin of the frame it is represented in and ends at the subscript. Including both unmodeled target acceleration and chaser accelerometer bias terms is crucial to prevent the bias in the chaser's accelerometer from being mistakenly attributed to an unmodeled target acceleration in the event that the target vehicle is experiencing unmodeled perturbations while the chaser vehicle is performing a maneuver.

MILTON, consists of three primary components: Propagation, measurement update, and an adaptive Block.

A. Propagation

In the propagation phase, each spacecraft state and its covariance are propagated independently. The relative inertial states of the target are converted to the full inertial representation prior to propagation and are converted back after. This conversion is done by,

$$\mathbf{r}_{t/c}^N = \mathbf{r}_t^N - \mathbf{r}_c^N \quad \mathbf{v}_{t/c}^N = \mathbf{v}_t^N - \mathbf{v}_c^N \,. \tag{2}$$

The states are propagated using a fixed step Runge-Kutta (RK4) propagator and the EKF propagation equations. The EKF is a widely utilized estimation algorithm in the aerospace industry, favored for its minimal computational demands. This computational ease stems from its use of first-order Taylor approximations [29]. These approximations are centered on the estimated state and thus the filter has the potential to diverge if the estimated state drifts too far from the truth. The EKF time propagation equations are,

$$\begin{aligned} &\dot{\mathbf{x}}_k = \mathbf{f}\left(\mathbf{x}_k^+, t\right), \quad \mathbf{P}_{k+1}^- = \mathbf{F}\mathbf{P}_k^+\mathbf{F}^T + \hat{\mathbf{Q}}, \\ &\mathbf{F} \approx \mathrm{e}^{(\mathbf{A}\Delta t)}, \qquad\quad \mathbf{A} = \left.\frac{\partial \mathbf{f}}{\partial \mathbf{x}}\right|_{\mathbf{x}_k^+}, \end{aligned} \tag{3}$$

where $\mathbf{x}$ is the state vector of size n, $\mathbf{f}()$ is the function that governs the state dynamics, t is time, $\mathbf{P}$ is the filter covariance estimate, $\mathbf{F}$ is the state transition matrix, and $\hat{\mathbf{Q}}$ is the discrete time process noise covariance matrix. The superscript, $()^-$, indicates that the quantity is the estimate prior to the measurement update and the superscript $()^+$, indicates that the quantity is the posterior estimate. The subscripts $()_k$ and $()_{k+1}$ indicate that the quantity is at time step k and $k+1$, respectively. It should be noted that $\mathbf{F} \approx \mathrm{e}^{(\mathbf{A}\Delta t)}$ is only an exact equivalency for a linear, time-invariant system, however this relationship is often leveraged for nonlinear systems to reduce computational burden. Once the conversion to the full inertial state is done, the states are propagated with,

$$\mathbf{f}(\mathbf{x}) = \dot{\mathbf{x}} = \begin{bmatrix} \dot{\mathbf{r}}_t^N \\ \dot{\mathbf{v}}_t^N \\ \dot{\mathbf{a}}_t^N \\ \dot{\mathbf{r}}_c^N \\ \dot{\mathbf{v}}_c^N \\ \dot{\mathbf{b}}_c^{B_c} \end{bmatrix} = \begin{bmatrix} \mathbf{v}_t^N \\ \mathbf{g}_t^N + \mathbf{a}_t^N \\ \boldsymbol{\nu}_t \\ \mathbf{v}_c^N \\ \mathbf{g}_t^N + \mathbf{N}\mathbf{B}_\mathbf{c}\left(\boldsymbol{\alpha}_c^{B_c} - \mathbf{b}_c^{B_c}\right) + \boldsymbol{\nu}_c \Delta t \\ -\beta \mathbf{b}^{B_c} + \boldsymbol{\nu}_b \end{bmatrix}, \tag{4}$$

where $\mathbf{g}$ is the acceleration of the spacecraft due to the gravity field, $\mathbf{NB_c}$ is the direction cosine matrix (DCM) from the chaser body frame to the inertial frame, $\boldsymbol{\alpha}_c$ is the measured acceleration from the chaser's onboard accelerometer, β is the inverse of the time constant for the Markov process of the accelerometer bias, and $\boldsymbol{\nu}$ is the process noise for various

terms. The acceleration, velocity, and position are directly related through kinematics. Since the acceleration on the target is unknown, it is assumed that the acceleration term is constant over each time step. It should be noted that while the noise term $\boldsymbol{\nu}_t$ appears in (4), there is no artificial noise added to either the true propagation or the filter propagation. This term serves as a placeholder for the assumed form the process noise adaptation expects model discrepancies to take. While there is no artificial noise added, there are true model discrepancies between the truth trajectories and the filter dynamics which vary from one scenario to the next. There are three separate sets of gravity field models used in this work. These three sets will be discussed in Section IV.

The covariances are propagated using (3) after constructing $\mathbf{A}$ using the following,

$$\mathbf{A} = \begin{bmatrix} \mathbf{A}_t & \mathbf{A}_{t/c} \\ \mathbf{0}_{9\times 9} & \mathbf{A}_c \end{bmatrix} \text{ where, } \quad \mathbf{A}_{t/c} = \begin{bmatrix} \mathbf{0}_{3\times 3} & \mathbf{0}_{3\times 3} & \mathbf{0}_{3\times 3} \\ \frac{\partial \mathbf{g}_t}{\partial \mathbf{r}_t} - \frac{\partial \mathbf{g}_c}{\partial \mathbf{r}_c} & \mathbf{0}_{3\times 3} & \mathbf{N}\mathbf{B}_c \\ \mathbf{0}_{3\times 3} & \mathbf{0}_{3\times 3} & \mathbf{0}_{3\times 3} \end{bmatrix}, \tag{5}$$

where $\mathbf{A}_t$ and $\mathbf{A}_c$ are the Jacobians of the dynamics of the target and chaser vehicles with respect to their states.

Maneuvers performed by the chaser are expected to be captured by the onboard accelerometer. Thus these accelerations are modeled as measurements from the accelerometer held constant over each propagation step. As previously mentioned, the bias term is necessary to avoid attributing sensor bias in the chaser to unmodeled accelerations in the target vehicle. Sensors often have bias values that vary over the length of a mission. This variability is often modeled as a Gauss-Markov process thus this study models its accelerometer bias as a Gauss-Markov process.

It should be noted that the accelerometer measurements are not always used directly in the propagation of the chaser vehicle. When the magnitude of the accelerometer reading is below a gating threshold, the measurements are not used in propagation, but instead are treated as direct measurements of the accelerometer bias terms [37]. This will be explained in more detail in the following section.

In the filter, the process noise on the relative target vehicle states is autonomously updated in the adaptive block. This will be discussed in greater detail in Section III.C. The process noise on the chaser vehicle is set at the beginning of the scenario and remains unchanged as it is not the focus of this work.

B. Measurement Update

In the measurement update, the EKF measurement update equations are used,

$$\begin{aligned} \mathbf{x}_{k+1}^{+} &= \mathbf{x}_{k+1}^{-} + \mathbf{K}\left(\mathbf{y}_{k+1} - \mathbf{h}\left(\mathbf{x}_{k+1}^{-}\right)\right), \quad \mathbf{K} = \mathbf{P}_{k+1}^{-}\mathbf{H}_{k+1}^{T}\left(\mathbf{H}_{k+1}\mathbf{P}_{k+1}^{-}\mathbf{H}_{k+1}^{T} + \mathbf{R}\right)^{-1} \\ \mathbf{P}_{k+1}^{+} &= \left(\mathbf{I} - \mathbf{K}\mathbf{H}_{k+1}\right)\mathbf{P}_{k+1}^{-}\left(\mathbf{I} - \mathbf{K}\mathbf{H}_{k+1}\right)^{T} + \mathbf{K}\mathbf{R}\mathbf{K}^{T}, \quad \mathbf{H}_{k+1} = \left.\frac{\partial \mathbf{h}}{\partial \mathbf{x}}\right|_{\mathbf{x}_{k+1}^{-}}, \end{aligned} \tag{6}$$

where $\mathbf{K}$ is the Kalman gain, $\mathbf{I}$ is the identity matrix, $\mathbf{y}_{k+1}$ is the received measurement of size m, $\mathbf{h}()$ is the measurement function that relates the state to the measurement, $\mathbf{H}$ is the measurement Jacobian, and $\mathbf{R}$ is the measurement noise covariance matrix. The EKF measurement update uses relative range and bearing measurements taken from the chaser to the target vehicle. These measurements are assumed to be provided by a flash LiDAR system. The relative range and bearing measurements are assumed to be in the center of the LiDAR frame, $\mathbf{L}$. The vector $\boldsymbol{\rho}^{\mathbf{L}}$ is the relative range vector defined in the LiDAR frame that defines the relative position of the target with respect to the chaser vehicle and can be found using,

$$\boldsymbol{\rho}^{L} = \mathbf{LN}\mathbf{r}_{t/c}, \tag{7}$$

where $\mathbf{LN}$ is the DCM from the inertial frame to the chaser LiDAR frame. The calculation of the relative range is performed as follows:

$$\rho = \left|\mathbf{r}^{\mathbf{N}}_{t/c}\right| = \left|\boldsymbol{\rho}^{\mathbf{L}}\right|. \tag{8}$$

The relative azimuth and elevation angles are calculated using,

$$\begin{aligned} A &= \arctan\left(\frac{\rho^{\mathbf{L}}_x}{\rho^{\mathbf{L}}_z}\right) \\ B &= \arctan\left(\frac{\rho^{\mathbf{L}}_y}{\rho^{\mathbf{L}}_z}\right). \end{aligned} \tag{9}$$

where $\rho^{\mathbf{L}}_x$, $\rho^{\mathbf{L}}_y$, and$\rho^{\mathbf{L}}_z$ are the components of the relative range vector in the LiDAR frame. This definition of the relative azimuth and elevation are used in order to mitigate angular quadrant assignment errors.

As previously mentioned, when the magnitude of the measurement taken by the accelerometer is below a gating threshold, the accelerometer measurement is taken to be a direct measurement of the accelerometer bias [37],

$$\mathbf{b}_c = \boldsymbol{\alpha}_c. \tag{10}$$

Thus the measurement Jacobian takes one of two forms during the measurement update:

$$\mathbf{H}_1 = \begin{bmatrix} \frac{1}{\rho}\mathbf{r}^T_{t/c} & \mathbf{0}_{1\times 15} \\ \frac{1}{\rho^2_x+\rho^2_z}[\rho_z, 0, -\rho_x]\mathbf{LN} & \mathbf{0}_{1\times 15} \\ \frac{1}{\rho^2_y+\rho^2_z}[0, \rho_z, -\rho_y]\mathbf{LN} & \mathbf{0}_{1\times 15} \end{bmatrix} \quad \text{or} \quad \mathbf{H} = \begin{bmatrix} \mathbf{H}_1 & \mathbf{0}_{3\times 15} \\ \mathbf{0}_{3\times 15} & \mathbf{I}_{3\times 3} \end{bmatrix}. \tag{11}$$

Since the goal is to estimate the relative state and since the absolute states are weakly observable from relative-only measurements, the chaser's position and velocity are treated as consider parameters [29]. This adjustment involves modifying the Kalman gain derived in (6), specifically by setting the values in the rows corresponding to the chaser's

position and velocity to zero,

$$\mathbf{K}_{\mathbf{r}_c^{\mathbf{N}},\mathbf{v}_c^{\mathbf{N}}} = 0\cdot \tag{12}$$

C. Process Noise Adaptation

The adaptation block employs correlation methods for process noise adaptation. In previous work on correlation methods, the theory has been applied to *linear* systems [7, 13, 15]. In this work, correlation methods are applied to a *nonlinear* system. In order to apply correlation methods to a nonlinear system, it is assumed that the time series of prefit measurement residuals in a buffer of length m_b are linearly related to the state error at the initial time in the buffer $k - m_b + 1$.

1. Derivation

Once making the assumption that the measurement residuals are linear with respect to the state error, the derivation follows the same steps laid out in [15], with the caveat that the matrices are Jacobians evaluated on the filter's best estimate of the state at that time step. In order to allow for self-containment, the rest of the derivation on the nonlinear system is included here. The linear relationship between the prefit measurement residuals in a buffer of length m_b and the state error at the initial time step in the buffer, $k - m_b + 1$ is as follows,

$$\underbrace{\begin{bmatrix} \mathbf{r}_k \\ \mathbf{r}_{k-1} \\ \vdots \\ \mathbf{r}_{k-m_b+1} \end{bmatrix}}_{=\mathcal{Y}_{k,k-m_b+1}} = \underbrace{\begin{bmatrix} \mathbf{H}_k\boldsymbol{\Phi}_{k,k-m_b+1} \\ \mathbf{H}_{k-1}\boldsymbol{\Phi}_{k-1,k-m_b+1} \\ \vdots \\ \mathbf{H}_{k-m_b+1} \end{bmatrix}}_{=\mathcal{O}_{k,k-m_b+1}} \mathbf{e}_{k-m_b+1}$$
$$+ \underbrace{\begin{bmatrix} \mathbf{H}_k & \mathbf{H}_k\mathbf{F}_{k-1} & \mathbf{H}_k\boldsymbol{\Phi}_{k,k-2} & \cdots & \mathbf{H}_k\boldsymbol{\Phi}_{k,k-m_b+2} \\ \mathbf{0}_{m\times n} & \mathbf{H}_{k-1} & \mathbf{H}_{k-1}\mathbf{F}_{k-2} & \cdots & \mathbf{H}_{k-1}\boldsymbol{\Phi}_{k-1,k-m_b+2} \\ \vdots & \vdots & \ddots & \vdots & \vdots \\ \mathbf{0}_{m\times n} & \mathbf{0}_{m\times n} & \mathbf{0}_{m\times n} & \mathbf{0}_{m\times n} & \mathbf{H}_{k-m_b+2} \\ \mathbf{0}_{m\times n} & \mathbf{0}_{m\times n} & \mathbf{0}_{m\times n} & \mathbf{0}_{m\times n} & \mathbf{0}_{m\times n} \end{bmatrix}}_{=\mathcal{M}^w_{k-1,k-m_b+1}} \underbrace{\begin{bmatrix} \boldsymbol{\nu}_{k-1} \\ \boldsymbol{\nu}_{k-2} \\ \vdots \\ \boldsymbol{\nu}_{k-m_b+1} \end{bmatrix}}_{=\mathcal{V}_{k-1,k-m_b+1}} + \underbrace{\begin{bmatrix} \boldsymbol{\eta}_k \\ \boldsymbol{\eta}_{k-1} \\ \vdots \\ \boldsymbol{\eta}_{k-m_b+1} \end{bmatrix}}_{=\mathcal{W}_{k,k-m_b+1}}, \tag{13}$$

where m_b is the buffer size, $\mathbf{r}_k$ is the measurement residual at time k, $\mathbf{e}_k$ is the state error at time k, $\mathbf{\Phi}_{k,k-m_b+1}$ is the discrete time state transition matrix from time step $k-m_b+1$ to k and $\boldsymbol{\nu}_k$ and $\boldsymbol{\eta}_k$ are random samples from the discrete time process noise and measurement noise respectively. Shown more compactly:

$$\mathcal{Y}_{k,k-m_b+1} = \mathcal{O}_{k,k-m_b+1}\mathbf{e}_{k-m_b+1} + \mathcal{M}^{w}_{k-1,k-m_b+1}\mathcal{V}_{k-1,k-m_b+1} + \mathcal{W}_{k,k-m_b+1}, \tag{14}$$

where $\mathcal{Y}$ is a vectorized time series of prefit measurement residuals, $\mathcal{O}$ is the observability matrix, $\mathcal{M}^{w}$ is the mapping matrix from the process noise samples to the measurement residuals, $\mathcal{V}$ is the vectorized time series of discrete time process noise samples, and $\mathcal{W}$ is the vectorized time series of discrete time measurement noise samples.

To isolate the state error vector, multiply both sides by $\mathcal{O}^{T}_{k,k-m_b+1}$ yielding,

$$\begin{aligned}\mathcal{O}^{T}_{k,k-m_b+1}\mathcal{Y}_{k,k-m_b+1} = \mathcal{M}_{k,k-m_b+1}\mathbf{e}_{k-m_b+1} &+\mathcal{O}^{T}_{k,k-m_b+1}\mathcal{M}^{w}_{k-1,k-m_b+1}\mathcal{V}_{k-1,k-m_b+1}\\ &+\mathcal{O}^{T}_{k,k-m_b+1}\mathcal{W}_{k,k-m_b+1},\end{aligned} \tag{15}$$

where $\mathcal{M}_{k,k-m_b+1}$ is the observability Gramian from time step $k-m_b+1$ to k. In this work, it is assumed that the observability Gramian is invertible. This assumption holds because the adaptation is being applied *only* to the relative target vehicle position, velocity, and unmodeled target acceleration states which are fully observable with relative range and bearing measurements from the chaser vehicle, as discussed in Section III.B. To isolate the state *errors*, multiply both sides of (15) by $\mathcal{M}^{-1}_{k,k-m_b+1}$,

$$\begin{aligned}\mathcal{M}^{-1}_{k,k-m_b+1}\mathcal{O}^{T}_{k,k-m_b+1}\mathcal{Y}_{k,k-m_b+1} = \mathbf{e}_{k-m_b+1} &+\mathcal{M}^{-1}_{k,k-m_b+1}\mathcal{O}^{T}_{k,k-m_b+1}\mathcal{M}^{w}_{k-1,k-m_b+1}\mathcal{V}_{k-1,k-m_b+1}\\ &+\mathcal{M}^{-1}_{k,k-m_b+1}\mathcal{O}^{T}_{k,k-m_b+1}\mathcal{W}_{k,k-m_b+1}.\end{aligned} \tag{16}$$

Suppose this vectorization is repeated for measurements taken from time step $k-m_b$ to $k-1$ yielding,

$$\begin{aligned}\mathcal{M}^{-1}_{k,k-m_b+1}\mathcal{O}^{T}_{k,k-m_b+1}\mathcal{Y}_{k,k-m_b+1} &= \mathbf{e}_{k-m_b+1} +\mathcal{M}^{-1}_{k,k-m_b+1}\mathcal{O}^{T}_{k,k-m_b+1}\mathcal{M}^{w}_{k-1,k-m_b+1}\mathcal{V}_{k-1,k-m_b+1}\\ &\quad +\mathcal{M}^{-1}_{k,k-m_b+1}\mathcal{O}^{T}_{k,k-m_b+1}\mathcal{W}_{k,k-m_b+1},\\ \mathcal{M}^{-1}_{k-1,k-m_b}\mathcal{O}^{T}_{k-1,k-m_b}\mathcal{Y}_{k-1,k-m_b} &= \mathbf{e}_{k-m_b} +\mathcal{M}^{-1}_{k-1,k-m_b}\mathcal{O}^{T}_{k-1,k-m_b}\mathcal{M}^{w}_{k-2,k-m_b}\mathcal{V}_{k-2,k-m_b}\\ &\quad +\mathcal{M}^{-1}_{k-1,k-m_b}\mathcal{O}^{T}_{k-1,k-m_b}\mathcal{W}_{k-1,k-m_b}.\end{aligned} \tag{17}$$

Now substitute $\mathbf{e}_{k-m_b+1} = \mathbf{F}_{k-m_b}\mathbf{e}_{k-m_b} + \boldsymbol{\nu}_{k-m_b}$ and subtract one equation from the other,

$$\mathcal{Z}_k = \mathcal{A}_k\mathcal{Y}_{k,k-m_b} = \mathcal{B}_k\mathcal{V}_{k-1,k-m_b} + \mathcal{A}_k\mathcal{W}_{k,k-m_b}, \tag{18}$$

where $\mathcal{A}_k$ is defined as,

$$\mathcal{A}_k = \left[\mathcal{M}^{-1}_{k,k-m_b+1}\mathcal{O}^T_{k,k-m_b+1}, \mathbf{0}_{n\times m}\right] - \left[\mathbf{0}_{n\times m}, \mathbf{F}_{k-m_b}\mathcal{M}^{-1}_{k-1,k-m_b}\mathcal{O}^T_{k-1,k-m_b}\right], \tag{19}$$

and $\mathcal{B}_k$ is defined as,

$$\mathcal{B}_k = \left[\mathcal{M}^{-1}_{k,k-m_b+1}\mathcal{O}^T_{k,k-m_b+1}\mathcal{M}^{w}_{k-1,k-m_b+1}, \mathbf{I}_{n\times n}\right] - \left[\mathbf{0}_{n\times n}, \mathbf{F}_{k-m_b}\mathcal{M}^{-1}_{k-1,k-m_b}\mathcal{O}^T_{k-1,k-m_b}\mathcal{M}^{w}_{k-2,k-m_b}\right], \tag{20}$$

yielding the 'measurement sequence' for correlation methods, $\mathcal{Z}$. Again, the definitions in (19) and (20) are identical to the quantities for a linear system in [15].

From here the autocorrelation $\mathbf{C}_{k,k-p}$, can be calculated as,

$$\mathbf{C}_{k,k-p} = \mathbb{E}\left[\mathcal{Z}_k\mathcal{Z}^T_{k-p}\right] = \sum_{i=p+1}^{m_b}\mathbf{B}^k_i\hat{\mathbf{Q}}\mathbf{B}^{k-p\,T}_{i-p} + \sum_{i=p}^{m_b}\mathbf{A}^k_i\mathbf{R}\mathbf{A}^{k-p\,T}_{i-p}. \tag{21}$$

The quantities $\mathbf{A}^{\mathbf{k}}_{\mathbf{i}}$ and $\mathbf{B}^{\mathbf{k}}_{\mathbf{i}}$ are defined as,

$$\begin{aligned}
\mathbf{A}_0 &= \mathcal{M}^{-1}_{k,k-m_b+1}\mathbf{\Phi}_{k,k-m_b+1}\mathbf{H}^T_k \\
\mathbf{A}_i &= \mathcal{M}^{-1}_{k,k-m_b+1}\mathbf{\Phi}_{k-i,k-m_b+1}\mathbf{H}^T_{k-i} - \mathbf{F}_{k-m_b}\mathcal{M}^{-1}_{k-1,k-m_b}\mathbf{F}^T_{k-m_b}\mathbf{\Phi}_{k-i,k-m_b+1}\mathbf{H}^T_{k-i} \\
\mathbf{A}_{m_b} &= -\mathbf{F}_{k-m_b}\mathcal{M}^{-1}_{k-1,k-m_b}\mathbf{F}^T_{k-m_b}\mathbf{H}^T_{k-m_b}
\end{aligned} \tag{22}$$

$$\begin{aligned}
\mathbf{B}_1 &= \mathcal{M}^{-1}_{k,k-m_b+1}\mathbf{\Phi}_{k,k-m_b+1}\mathcal{M}_{k,k} \\
\mathbf{B}_j &= \mathcal{M}^{-1}_{k,k-m_b+1}\mathbf{\Phi}_{k-i,k-m_b+1}\mathcal{M}_{k,k-i+1} - \mathbf{F}_{k-m_b}\mathcal{M}^{-1}_{k-1,k-m_b}\mathbf{\Phi}^T_{k-i,k-m_b}\mathcal{M}_{k-1,k-i+1} \\
\mathbf{B}_{m_b} &= \mathbf{I}_{n\times n} - \mathbf{F}_{k-m_b}\mathcal{M}^{-1}_{k-1,k-m_b}\mathbf{F}^T_{k-m_b}\mathcal{M}_{k-1,k-m_b+1}
\end{aligned} \tag{23}$$

noting that $\mathbf{A}_i$ is defined on the interval $i \in [0, m_b]$ while $\mathbf{B}_j$ on the interval $j \in [1, m_b]$. Written differently (21) becomes [15],

$$\underbrace{\begin{bmatrix} \text{vech}\left(\hat{\mathbf{C}}_{k,k}\right) \\ \text{vec}\left(\hat{\mathbf{C}}_{k,k-1}\right) \\ \vdots \\ \text{vec}\left(\hat{\mathbf{C}}_{k,k-m_b}\right) \end{bmatrix}}_{=\hat{\mathbf{c}}_k} = \underbrace{\begin{bmatrix} \sum_{i=1}^{m_b}\mathbf{B}^k_i \otimes_h \mathbf{B}^k_i & \sum_{i=0}^{m_b}\mathbf{A}^k_i \otimes_h \mathbf{A}^k_i \\ \sum_{i=2}^{m_b}\mathbf{B}^{k-1}_{i-1} \otimes_u \mathbf{B}^k_i & \sum_{i=1}^{m_b}\mathbf{A}^{k-1}_{i-1} \otimes_u \mathbf{A}^k_i \\ \vdots & \vdots \\ \sum_{i=m_b+1}^{m_b}\mathbf{B}^{k-m_b-1}_{i-m_b-1} \otimes_u \mathbf{B}^k_i & \sum_{i=m_b}^{m_b}\mathbf{A}^{k-m_b}_{i-m_b} \otimes_u \mathbf{A}^k_i \end{bmatrix}}_{=\mathbf{D}_k} \underbrace{\begin{bmatrix} \text{vech}\left(\hat{\mathbf{Q}}\right) \\ \text{vech}\left(\mathbf{R}\right) \end{bmatrix}}_{=\boldsymbol{\theta}_k}, \tag{24}$$

where $\hat{C}$ is the 'measured' autocorrelation, and vech() and vec() are defined as,

$$\mathbf{R} = \begin{bmatrix} r_{11} & r_{12} & r_{13} \\ r_{21} & r_{22} & r_{23} \\ r_{31} & r_{32} & r_{33} \end{bmatrix}, \quad \begin{aligned} \text{vec}\left(\mathbf{R}\right) &= \begin{bmatrix} r_{11} & r_{12} & r_{13} & r_{21} & r_{22} & r_{23} & r_{31} & r_{32} & r_{33} \end{bmatrix}^T, \\ \text{vech}\left(\mathbf{R}\right) &= \begin{bmatrix} r_{11} & r_{12} & r_{13} & r_{22} & r_{23} & r_{33} \end{bmatrix}^T, \end{aligned} \tag{25}$$

and $\otimes$ represents a Kroneker product with the known property $\text{vec}\left(\mathbf{AXB}\right) = \left(\mathbf{B}^T \otimes \mathbf{A}\right) \text{vec}(\mathbf{X})$. When the central matrix, $\mathbf{X}$, is symmetric a special Kroneker product relationship is defined as $\text{vec}\left(\mathbf{AXB}\right) = \left(\mathbf{B}^T \otimes_u \mathbf{A}\right) \text{vech}(\mathbf{X})$. When the central matrix, $\mathbf{X}$, is symmetric and is multiplied by the same matrix on either side, this relationship can be written as $\text{vech}\left(\mathbf{AXA^T}\right) = \left(\mathbf{A} \otimes_h \mathbf{A}\right) \text{vech}(\mathbf{X})$. From here, the system of equations in (24) can be used to estimate the process noise and measurement noise of the system.

The work presented here is focused on adapting to model discrepancies in the dynamics, thus the measurement noise is assumed to be know and the following adjustment is made to (24),

$$\hat{\mathbf{c}}_k - \begin{bmatrix} \sum_{i=0}^{m_b} \mathbf{A}_i^k \otimes_h \mathbf{A}_i^{kT} \\ \sum_{i=1}^{m_b} \mathbf{A}_{i-1}^{k-1} \otimes_u \mathbf{A}_i^{kT} \\ \vdots \\ \sum_{i=m_b}^{m_b} \mathbf{A}_{i-m_b}^{k-m_b} \otimes_u \mathbf{A}_i^{kT} \end{bmatrix} \text{vech}\left(\mathbf{R}\right) = \begin{bmatrix} \sum_{i=1}^{m_b} \mathbf{B}_i^k \otimes_h \mathbf{B}_i^{kT} \\ \sum_{i=2}^{m_b} \mathbf{B}_{i-1}^{k-1} \otimes_u \mathbf{B}_i^{kT} \\ \vdots \\ \sum_{i=m_b+1}^{m_b} \mathbf{B}_{i-m_b-1}^{k-m_b-1} \otimes_u \mathbf{B}_i^{kT} \end{bmatrix} \text{vech}\left(\hat{\mathbf{Q}}\right). \tag{26}$$

2. Maintaining Definiteness of the Process Noise Covariance Matrix

Examining (24) and (25) reveals that the estimation of the upper triangular entries of the noise matrices guarantees symmetry. However, enforcing symmetry does not ensure positive definiteness. For the covariance matrix of the state estimate to remain positive definite, the process noise covariance matrix must also be positive definite. Early studies address this challenge heuristically; they opt simply to not update the estimate when positive definiteness is compromised [7, 38]. More recently, [15] approaches this issue by using Riemann manifolds to estimate the noise matrices for linear systems. While this method effectively ensures positive definiteness, it is computationally demanding, posing significant challenges for deployment onboard a spacecraft.

In order to provide a guarantee of positive definiteness without employing ad hoc methods or computationally demanding methods this work a few assumptions are made. First, MILTON assumes that the process noise acts as a random jerk sampled from a zero mean distribution with a continuous time covariance matrix $\mathbf{Q}$ and applied as a zero order hold over the propagation interval Δt. This creates a relationship between the continuous time process noise and

the discrete time process noise [39],

$$\hat{\mathbf{Q}} = \begin{bmatrix} \frac{\Delta t^5}{20}\mathbf{Q} & \frac{\Delta t^4}{8}\mathbf{Q} & \frac{\Delta t^3}{6}\mathbf{Q} \\ \frac{\Delta t^4}{8}\mathbf{Q} & \frac{\Delta t^3}{3}\mathbf{Q} & \frac{\Delta t^2}{2}\mathbf{Q} \\ \frac{\Delta t^3}{6}\mathbf{Q} & \frac{\Delta t^2}{2}\mathbf{Q} & \Delta t\mathbf{Q} \end{bmatrix}. \tag{27}$$

In the truth trajectory generation, there is no 'artificial' noise that behaves according to this assumption. However, this assumption allows for the usage of kinematics to relate unknown perturbations in the propagation of the unmodeled target acceleration to the relative position and velocity uncertainty. Each scenario has its own set of model mismatches between the 'true' dynamics and the filter model dynamics, but each perturbation causes a change in the dynamics that enters through the unmodeled target acceleration and obeys kinematic motion. Leveraging the kinematic relationship between the vehicle states is one of the improvements implemented to improve upon previous work with correlation methods because it enforces a realistic relationship between the target state uncertainties. Additionally, when the matrix $\mathbf{Q}$ is positive definite, $\hat{\mathbf{Q}}$ will also be positive definite.

So far, these assumptions ensure symmetry and now physical meaning, but not positive definiteness. Another common assumption is that the continuous time process noise power spectral density is a diagonal matrix in some strategically chosen frame [40, 41], such as the local vertical local horizontal frame. To ensure positive definiteness, MILTON estimates the component-wise square root of the continuous time process noise power spectral density. These changes result in the following system of equations,

$$\begin{aligned} \hat{\mathbf{c}}_k &= \hat{\mathbf{D}}_k \mathbf{s}_k \quad \mathbb{Q} = \frac{\partial \mathbf{Q}_{\text{diag}}}{\partial \mathbf{s}_k}, \\ \hat{\mathbf{c}}_k &= \begin{bmatrix} \text{vech}\left(\hat{\mathbf{C}}_{k,k}\right) \\ \text{vec}\left(\hat{\mathbf{C}}_{k,k-1}\right) \\ \vdots \\ \text{vec}\left(\hat{\mathbf{C}}_{k,k-m_b}\right) \end{bmatrix} - \begin{bmatrix} \sum_{i=0}^{m_b} \mathbf{A}_i^k \otimes_h \mathbf{A}_i^{kT} \\ \sum_{i=1}^{m_b} \mathbf{A}_{i-1}^{k-1} \otimes_u \mathbf{A}_i^{kT} \\ \vdots \\ \sum_{i=m_b}^{m_b} \mathbf{A}_{i-m_b}^{k-m_b} \otimes_u \mathbf{A}_i^{kT} \end{bmatrix} \text{vech}\left(\mathbf{R}\right), \\ \hat{\mathbf{D}}_k &= \begin{bmatrix} \sum_{i=1}^{m_b} \mathbf{B}_i^k \otimes_h \mathbf{B}_i^{kT} \\ \sum_{i=2}^{m_b} \mathbf{B}_{i-1}^{k-1} \otimes_u \mathbf{B}_i^{kT} \\ \vdots \\ \sum_{i=m_b+1}^{m_b} \mathbf{B}_{i-m_b-1}^{k-m_b-1} \otimes_u \mathbf{B}_i^{kT} \end{bmatrix} \mathbb{D}\mathbb{Q}, \end{aligned} \tag{28}$$

where $\mathbf{s}_k$ is the square root of the continuous time process noise power spectral density diagonal, $\mathbb{D}$ is the matrix that transforms the continuous time process noise power spectral density diagonal to the upper triangular of the discrete time process noise power spectral density governed by (27), and $\mathbb{Q}$ is the derivative of the continuous time process noise

diagonal with respect to the square root of that diagonal. With this new measurement model for the adaptation, both symmetry and positive definiteness are guaranteed. Assuming a diagonal power spectral density matrix is very common in manual tuning; this approach combined with (27) produces a realistic and positive definite, discrete time process noise covariance matrix without having to employ computationally burdensome or ad hoc overwriting techniques.

3. Implementation Updates

In [7, 13, 15], the correlation method systems of equations are used in a recursive least squares framework with an initial estimate $\hat{\boldsymbol{\theta}}_0$ and covariance matrix of that estimate, $\boldsymbol{\Psi}_0$. To solve (28), in traditional recursive least squares for this system, one must invert a matrix of size $m_b n^2 + \frac{(n+1)n}{2} \times m_b n^2 + \frac{(n+1)n}{2}$. In the work presented here, $n = 9$ and m_b varies. This means the inversion required to solve the standard least squares setup would minimally be 126×126 for a buffer size of $m_b = 1$. Clearly, this inversion poses a significant computational burden. By converting the recursive least squares to an information form allows for the largest inversion to be the size of $\boldsymbol{\Psi}$, or in terms of this system a 3×3.

Due to the size of the state space in this work, this is a major improvement upon previous works as this change allows for larger buffers to be considered. This helps to mitigate the effects of outliers on the estimate of the process noise. As the buffer size increases, the accuracy of the estimate of the process noise produced should increase as well. The equations that govern the information form are [29],

$$
\begin{aligned}
\boldsymbol{\Lambda}_k^+ &= \left(\boldsymbol{\Psi}_k^+\right)^{-1}, \quad \mathbf{d}_k^+ = \boldsymbol{\Lambda}_k^+ \mathbf{s}_k^+, \\
\boldsymbol{\Lambda}_{k+1}^- &= \left(\mathbf{I}_{3\times 3} - \boldsymbol{\Lambda}_k^+ \left(\boldsymbol{\Lambda}_k^+ + \mathbf{Q}_w^{-1}\right)^{-1}\right) \boldsymbol{\Lambda}_k^+, \\
\mathbf{d}_{k+1}^- &= \left(\mathbf{I}_{3\times 3} - \boldsymbol{\Lambda}_k^+ \left(\boldsymbol{\Lambda}_k^+ + \mathbf{Q}_w^{-1}\right)^{-1}\right) \mathbf{d}_k^+, \\
\mathbf{d}_{k+1}^+ &= \mathbf{d}_{k+1}^- + \hat{\mathbf{D}}_{k+1}^T \mathbf{R}_w^{-1} \hat{\mathbf{c}}_{k+1}, \\
\boldsymbol{\Lambda}_{k+1}^+ &= \boldsymbol{\Lambda}_{k+1}^- + \hat{\mathbf{D}}_{k+1}^T \mathbf{R}_w^{-1} \hat{\mathbf{D}}_{k+1},
\end{aligned}
\tag{29}
$$

where $\mathbf{d}$ is the information state, $\boldsymbol{\Lambda}$ is the information matrix, and $\mathbf{Q}_w$ and $\mathbf{R}_w$ are the process noise and measurement noise for the adaptation itself. In this work, the adaptation process noise and measurement noise are assumed to be constant and thus their inversions can be calculated offline. A final implementation note is that the information update is not run every time step, but instead is only called when the buffer of measurements, $\hat{\mathbf{c}}_k$ is full of completely new measurements, or once every $m_b + 1$ time steps. With the changes detailed in this section, this algorithm is capable of guaranteeing a positive definite process noise covariance matrix for the nonlinear scenario of onboard relative navigation with full relative state observability.

IV. Numerical Results

This section covers the numerical results for two use cases for MILTON. In each scenario, there is a crewed target vehicle. For crewed missions, it is important to consider the impacts of the crew life support system on the spacecraft. To maintain the health of the crew the life support system performs regular vents to reduce the level of CO_2 gas onboard and eliminate waste water. Accounting for crew related vents has been a recent concern for NASA's Artemis II mission [4]. The vents in this work are modeled after information released from NASA on Gateway [42–44]. The vents are applied according to Table 1 and are modeled as discrete 'on' or 'off' in the true dynamics.

Table 1 Venting information, assumes the spacecraft mass is 39000kg [42]

Vent Type	Frequency	1σ Magnitude $\left[m/s^2\right]$	Duration $[s]$	Body Frame Direction
CO_2	every 10 min	1.7094e-5	10	$[-0.5, -0.866, 0]^T$
Waste Water	every 6 hours	1.8803e-05	60	$[-0.5, 0, -0.866]^T$

The Artemis II mission will have periods of operation in low Earth orbit and in cislunar space. Thus in the first scenario, there is a difference in the order zonal harmonic used to simulate the gravity field of the Earth in addition to unmodeled target vehicle CO_2 and waste water vents. In the second scenario, the two spacecraft are placed in Near Rectilinear Halo Orbits (NRHOs) governed by the Circular Restricted Three Body Problem (CR3BP) where the target vehicle is experiencing unmodeled CO_2 and waste water vents.

In both scenarios, it is assumed that there are measurements received every second from a flash LiDAR and an accelerometer on board the chaser vehicle. It is assumed that the LiDAR has a 128x128 pixel array and a 5° field of view [45]. The measurement covariance matrix is,

$$\mathbf{R}_1 = \begin{bmatrix} (0.08m)^2 & 0 & 0 \\ 0 & (0.04°)^2 & 0 \\ 0 & 0 & (0.04°)^2 \end{bmatrix} \quad \text{or} \quad \mathbf{R}_2 = \begin{bmatrix} \mathbf{R}_1 & \mathbf{0}_{3\times1} \\ \mathbf{0}_{1\times3} & (3.433\text{e-}6\mathbf{I}_{3\times3}m/s^2/\sqrt{s})^2 \end{bmatrix}, \tag{30}$$

these values reflect the uncertainty of the LiDAR used for the Osiris-REx mission [46] and an accelerometer.

The accelerometer gating threshold is set to be 1e-4 m/s^2. When the accelerometer measurement has a magnitude below the threshold, the measurement is treated as a direct measurement of the chaser accelerometer bias and R_2 is used. When the accelerometer measurement has a magnitude above the gating threshold, it is assumed that the chaser vehicle is maneuvering and the measurement is processed and used as a chaser acceleration. The accelerometer bias is modeled as a Gauss-Markov process with the inverse of the time constant set to be $\beta = 3600^{-1}s^{-1}$ with an initial bias of 2.9430e-5 m/s^2 for each axis. The velocity random walk is assumed to be 3.433e-6 $m/s^2/\sqrt{s}$. The discrete time process noise matrix for the chaser accelerometer bias is set to be 3.433e-8$\mathbf{I}m/s^2$.

For each scenario a 100 run Monte Carlo simulation is conducted. The results presented are comprised of error and

error interval estimates comparing the sample 3σ error intervals with the predicted 3σ error intervals from MILTON. The sample average error is calculated by taking the mean of the errors across Monte Carlo runs,

$$\bar{\mathbf{e}}_k^+ = \frac{1}{N_{\text{MC}}} \sum_{i=1}^{N_{\text{MC}}} \mathbf{e}_k^{i+} = \frac{1}{N_{\text{MC}}} \sum_{i=1}^{N_{\text{MC}}} (\hat{\mathbf{x}}_k^{i+} - \mathbf{x}_k^i), \tag{31}$$

where N_{MC} is the number of Monte Carlo runs ($N_{\text{MC}} = 100$), $\hat{\mathbf{x}}_k^{i+}$ is the posterior estimated state from the ith Monte Carlo run at time step k, and $\mathbf{x}_k^i$ is the truth state from the ith Monte Carlo run at time step k. It should be noted that the $\hat{}$ is used in the above equation to clearly delineate between the estimated state and the true state. This quantity is used to calculate the sample 3σ intervals, $\mathbf{P}_k^+$,

$$\mathbf{P}_k^+ = \frac{1}{N_{\text{MC}}} \sum_{i=1}^{N_{\text{MC}}} \mathbf{e}_k^{i+} \mathbf{e}_k^{i+T}. \tag{32}$$

The sample intervals are compared with the estimated 3σ intervals from MILTON. Since the process noise is adapted independently for each run the runs produce separate uncertainty estimates. To simplify the results, the estimated 3σ intervals are averaged together across Monte Carlo runs,

$$\bar{\mathbf{P}}_k^+ = \frac{1}{N_{\text{MC}}} \sum_{i=1}^{N_{\text{MC}}} \hat{\mathbf{P}}_k^{i+}, \tag{33}$$

where $\hat{\mathbf{P}}_k^{i+}$ is the estimated posterior covariance matrix of the ith Monte Carlo run at time step k.

There are three primary frames that the results of this study are presented in: inertial, body, and RTN. The inertial frame is Earth centered with the z axis aligned with the Earth spin axis. The body frame is fixed with respect to each spacecraft. It is assumed that both spacecraft are oriented such that their y axes are aligned with the relative position vector to the other vehicle. It is also assumed that the LiDAR is oriented with the boresight aligned with the spacecraft y axis, towards the other vehicle. The body z axes are assumed to be normal to the relative motion and the relative position, and the x axis completes the triad. The RTN frame is the radial, transverse, normal frame and is defined such that the radial direction is aligned with the inertial position vector, the normal is defined in the direction of the orbit normal, and the transverse completed the triad [47].

To evaluate whether the adaptation is functioning effectively, several key indicators are examined. First, the average error line should be approximately zero throughout the scenario, indicating that the filter is producing unbiased results. Second, the individual Monte Carlo simulations should largely fall within the average estimated 3σ intervals set by MILTON. Last, there should be a close match between the average estimated 3σ intervals from MILTON and the sample 3σ.

It should be noted that the state error plots for the chaser vehicle are not included, as these states are treated as

consider parameters and are not updated. Additionally, the initial portions of the results, where the filter error rapidly decreases, are omitted to provide better resolution in the latter portion of the scenarios.

A. Earth Gravitational Model Difference and Target Vehicle Venting

In this scenario, the crewed target vehicle and unmanned chaser vehicle operate in Earth orbits. There are two separate gravity models used in this simulation: one to generate the true spacecraft trajectory, one to propagate the estimated state in the filter itself. The gravity model used to propagate the true state includes two body dynamics with $J_2 - J_6$ zonal harmonic perturbations. While the gravity model used in the filter propagation includes two body dynamics with $J_2 - J_4$ only,

$$\begin{aligned} \mathbf{g}_{\text{truth}} &= \mathbf{g}_{\text{TBP}} + \sum_{i=2}^{6} \mathbf{g}_{J_i}, \\ \mathbf{g}_{\text{filter}} &= \mathbf{g}_{\text{TBP}} + \sum_{i=2}^{4} \mathbf{g}_{J_i}. \end{aligned} \tag{34}$$

Both of these models are derived using the Legendre polynomials and the gravity potential from [47]. The numeric values used in (34) can be found in Table 2. For clarity, the target vehicle and chaser vehicle truth trajectories are both propagated independently with the $\mathbf{g}_{\text{truth}}$ gravity model. In the filter, both spacecraft are propagated independently with $\mathbf{g}_{\text{filter}}$. As mentioned previously, there is a limit to the complexity of the dynamics model that a spacecraft can implement onboard, an thus there is always a degree of model discrepancy between the truth and the modeled dynamics. Two separate gravity models are used here to emulate this difference in a scaled down fashion.

Table 2 Earth constants used in propagation.

Parameter	$\mu\ [m^3/s^2]$	$R_{Earth}[m]$	$J_2[-]$	$J_3[-]$	$J_4[-]$	$J_5[-]$	$J_6[-]$
Value	3.986e14	6.378e6	1.083e-3	-2.532e-6	-1.620e-6	-2.278e-7	5.407e-7

The vehicles in this scenario start in separate orbits with the ultimate goal of the chaser vehicle maneuvering to rendezvous with the venting target. The simulation length of each Monte Carlo for the venting scenario is 5680s. There are ten vents total over this simulation period, nine of which are CO_2 vents and just one waste water vent. The initial CO_2 vent start time is randomized for each Monte Carlo using a discrete uniform distribution to begin between 100s and 300s from the beginning of the simulation. Each of the following CO_2 vents occurs on the frequency listed in Table 1. The waste water vent occurs 1400s after the initial CO_2 vent. Each of the vent magnitudes are similarly randomized by sampling from a normal distribution centered on zero with the 1σ magnitudes in Table 1. To maintain the direction of the vents the absolute value of these samples are used. Information on the chaser vehicle's maneuver to capture can be seen in Table 3.

Each truth trajectory is generated by back propagating from desired rendezvous final conditions of $[\mathbf{r}_{t/c}^T \mathbf{v}_{t/c}^T]^T =$

Table 3 Burn information for the chaser vehicle.

Vehicle	Burn Start $[s]$	Burn Length $[s]$	Magnitude $\left[m/s^2\right]$	Inertial Direction
Chaser	5560	30	1.0e-2	$[-0.7071, -0.7071, 0.00]^T$

$[-\mathbf{1}_{1x3}m, \mathbf{0}_{1x3}]^T$ while applying a the chaser capture maneuver and randomly sampled target vents. The true final Keplerian elements for the two spacecraft can be found in Table 4.

Table 4 Final Keplerian elements for the venting scenario.

Element	$a[m]$	$e[-]$	$inc[^\circ]$	$\Omega[^\circ]$	$\omega[^\circ]$	$M_f[^\circ]$
Target	6.878e6	0.000	15.00	0.000	0.000	5.000e-6
Chaser	6.878e6	2.300e-7	15.00	0.000	309	50.77

The filter in each Monte Carlo run is initialized by randomly sampling from a normal distribution centered on the true initial state with an initial covariance matrix for each spacecraft of,

$$\mathbf{P}_0 = \begin{bmatrix} \left(\frac{25}{3}\right)^2 \mathbf{I}_{3\times3} & \mathbf{0}_{3\times3} & \mathbf{0}_{3\times3} \\ \mathbf{0}_{3\times3} & \left(\frac{1}{10}\right)^2 \mathbf{I}_{3\times3} & \mathbf{0}_{3\times3} \\ \mathbf{0}_{3\times3} & \mathbf{0}_{3\times3} & (1\text{e-}9)^2\mathbf{I}_{3\times3} \end{bmatrix}, \tag{35}$$

where the position, velocity, and acceleration are in the units m, m/s, and m/s^2. The initial uncertainty reflects that the vehicles have just lost GPS just prior to the scenario start.

Measurements are received every second and the accelerometer gating threshold is set to be 1e-4 m/s^2 and the accelerometer bias time inverse of the time constant set to be $\beta = 3600^{-1}s^{-1}$ with a true initial bias of 2.9430e-6 m/s^2 for each axis. The velocity random walk is assumed to be 3.434e-6 $m/s^2/\sqrt{s}$.

The initial square root of the process noise diagonal, $\mathbf{s}_{t,0}$, for the target vehicle is randomized for each MC run by sampling from a normal distribution centered around $\mathbf{s}_{t,0}$ = 1e-6$\mathbf{1}_{3\times1}$, with a covariance matrix, $\mathbf{\Psi}_0$ = 1e-3$\mathbf{I}_{3\times3}$. The adaptation is initialized with this same random value. The adaptation buffer is set to be $m_b = 30$ and the adaptation process noise and measurement noise are set to be $\mathbf{Q}_w$ = 1e-5$\mathbf{I}_{3\times3}$ and $\mathbf{R}_w$ = 1$\mathbf{I}$ respectively. The process noise covariance matrix in the filter for the chaser vehicle dynamics is set to be $\mathbf{Q}_c$ = 1e-12$\mathbf{I}_{3\times3}$. The discrete time process noise matrix for the chaser accelerometer bias is set to be 3.433e-8$\mathbf{I}m/s^2$.

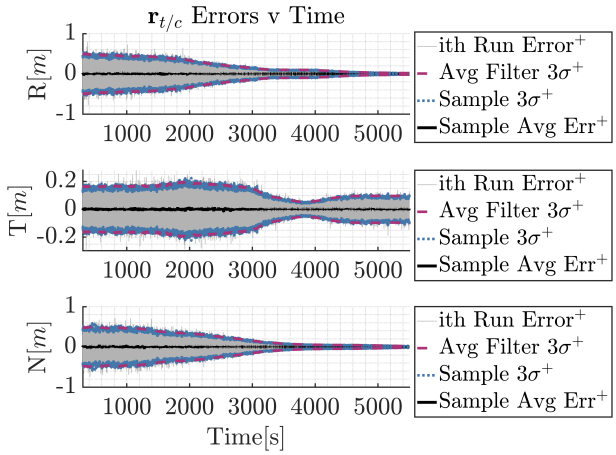

Fig. 1 Relative position of the target vehicle errors in the target RTN frame versus time excluding initial 300s.

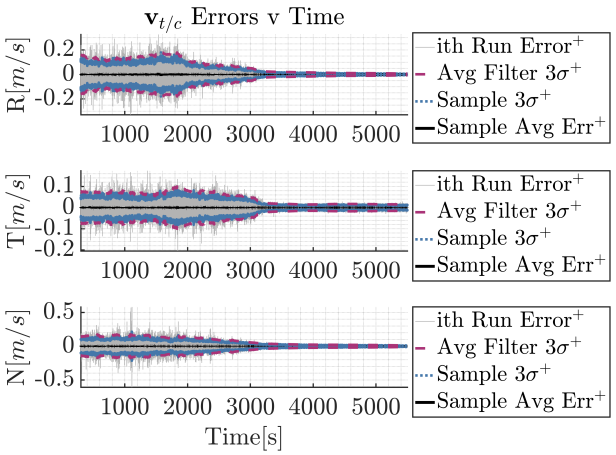

Fig. 2 Relative velocity of the target vehicle errors in the target RTN frame versus time excluding initial 300s.

It is clear that the adaptation successfully compensates for the unknown, regular venting by examining the average $3\sigma^+$ intervals compared with the sample $3\sigma^+$ intervals in Figure 1. While the estimated intervals in Figures 2 and 3 overestimate the errors in the relative velocity and acceleration, the intervals for the relative position nearly overlay the sample estimates.

To further confirm that the filter is functioning properly, the prior measurement residuals and their 3σ intervals are shown in Figures 5 and 6. The relative elevation errors spike toward the end of the simulation when the chaser vehicle maneuvers to capture with the target vehicle. This is due to the angular sensitivity becoming heightened as the two spacecraft come close to one another. The process noise adaptation allows the uncertainty intervals to grow with the measurement residuals, thus allowing the errors in the filter to remain well contained between the estimated intervals. Figure 4 is included to demonstrate that the chaser accelerometer bias is able to be estimated directly during the scenario when no chaser maneuver is occurring, which allows for an accurate estimate of the chaser accelerometer bias for times when the chaser vehicle does perform a maneuver.

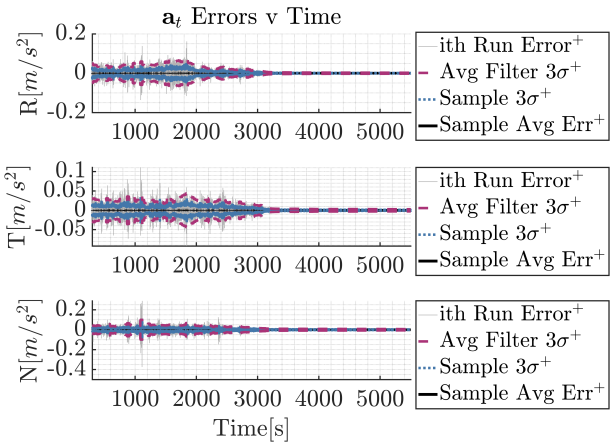

Fig. 3 Unmodeled acceleration of the target vehicle errors in the target RTN frame versus time excluding initial 300s.

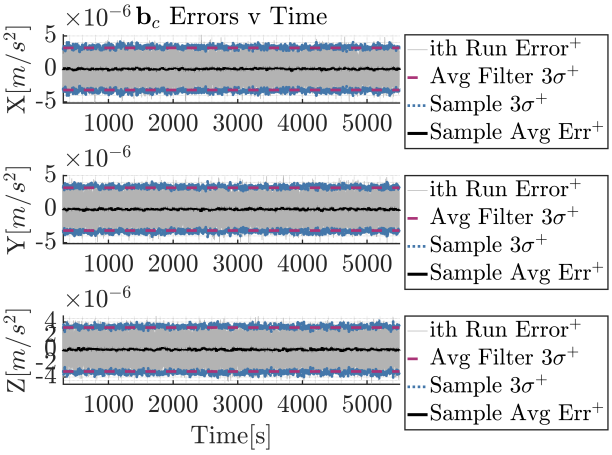

Fig. 4 Chaser accelerometer bias errors in the chaser body frame versus time excluding initial 300s.

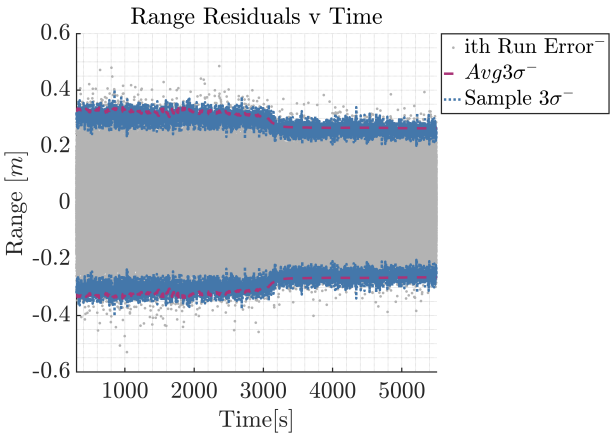

Fig. 5 Range measurement residuals versus time excluding initial 300s.

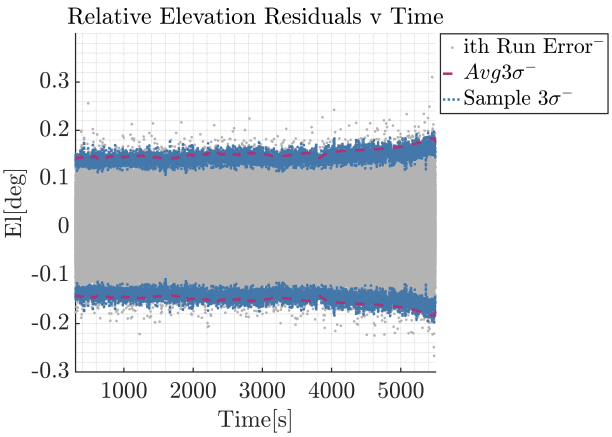

Fig. 6 Elevation measurement residuals versus time excluding initial 300s.

B. NRHO Target Vehicle Venting

In this scenario, similar to the previous scenario, the target and chaser vehicle start in separate orbits with the ultimate goal of the chaser vehicle maneuvering to rendezvous with a venting target vehicle. The fundamental difference between the previous scenario and this one is that the two spacecraft are operating in cislunar space with the destination orbit being an NRHO as shown in Figure 7.

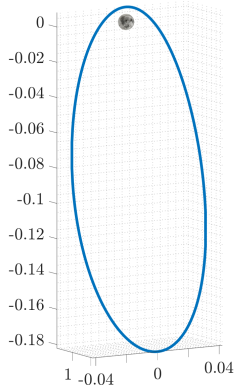

Fig. 7 Desired final orbit trajectory plotted in the rotating frame centered on the barrycenter of the Earth and Moon.

The gravitational model used for both the true and the filter dynamics is the Circular Restricted Three Body Problem,

$$\mathbf{g}_{\text{CR3BP}} = \begin{bmatrix} 2v_y + r_x - \frac{(1-\mu_{\text{CR3BP}})(r_x+\mu_{\text{CR3BP}})}{(r_1)^3} - \frac{\mu_{\text{CR3BP}}(r_x-1+\mu_{\text{CR3BP}})}{(r_2)^3} \\ -2v_x + r_y - \frac{(1-\mu_{\text{CR3BP}})r_y}{r_1^3} - \frac{\mu_{\text{CR3BP}}r_y}{r_2^3} \\ \frac{-(1-\mu_{\text{CR3BP}})r_z}{r_1} - \frac{\mu_{\text{CR3BP}}r_z}{r_2^3} \end{bmatrix} \tag{36}$$

$$r_1 = \sqrt{(r_x+\mu_{\text{CR3BP}})^2 + r_y^2 + r_z^2} \quad r_2 = \sqrt{(r_x-1+\mu_{\text{CR3BP}})^2 + r_y^2 + r_z^2}$$

where μ_{CR3BP} is the mass ratio between the Earth and the Moon and the state components are represented in the nondimensional rotating frame. The truth and the filter both operate in the nondimensional and rotating frame centered on the barycenter of the Earth and Moon. The final results are converted to dimensional units and shown in the RTN frame for ease of comparison with the other scenarios. Table 5 shows the constants used to nondimensionalize the state and propagate.

Table 5 Conversion and propagation constants.

Element	$\mu_{\text{CR3BP}}[-]$	Characteristic Time [s]	Characteristic Length [m]
Value	1.215e-2	3.752e5	3.844e8

The simulation length is 5500s for the NRHO target vehicle venting scenario. The truth trajectories are made in a similar fashion to the previous scenario. Each truth trajectory is generated by back propagating from desired rendezvous final conditions of $\left[\left(\mathbf{r}_{t/c}^N\right)^T \left(\mathbf{v}_{t/c}^N\right)^T\right]^T = 2[-\mathbf{1}_{1x3}, \mathbf{0}_{1x3}]^T$ while applying a the chaser capture maneuver and randomly sampled target vents. The target vents are applied in this scenario are also based on the information in Table 1. The true final nondimensional and rotating states for the two spacecraft can be found in table 7. The chaser vehicle maneuver to capture based on the information in Table 6.

Table 6 Burn information for the chaser vehicle.

Vehicle	Burn Start $[s]$	Burn Length $[s]$	Magnitude $\left[m/s^2\right]$	Inertial Direction
Chaser	5470	30	1.0e-2	$[-0, 1, 0]^T$

Table 7 Final nondimensional and rotating states for the NRHO venting scenario.

Relative Target	-7.357e-9	-1.399e-10	-5.203e-9	-1.399e-10	7.357e-9	0.000
Chaser	0.9879	1.432e-2	2.009e-3	7.173e-2	0.9238	-0.8528

The filter in each run is initialized by randomly sampling from a normal distribution centered on the true initial state with a covariance matrix of,

$$\mathbf{P}_0 = \begin{bmatrix} (\text{2.5e-8})^2\,\mathbf{I}_{3\times3} & \mathbf{0}_{3\times3} & \mathbf{0}_{3\times3} \\ \mathbf{0}_{3\times3} & (\text{2.5e-11})^2\,\mathbf{I}_{3\times3} & \mathbf{0}_{3\times3} \\ \mathbf{0}_{3\times3} & \mathbf{0}_{3\times3} & (\text{3.5e-7})^2\mathbf{I}_{3\times3} \end{bmatrix}, \tag{37}$$

for each spacecraft. Each of the entries is nondimensional and the covariance is represented in the rotating frame. Measurements are received every second and the same accelerometer gating and bias are used as in the previous scenarios, only in this scenario the units are converted to be nondimensional.

The initial square root of the process noise diagonal, $\mathbf{s}_{t,0}$, for the target vehicle is randomized for each MC run by sampling from a normal distribution centered around $\mathbf{s}_{t,0} = \text{1e-6}\mathbf{1}_{3\times1}$, with a covariance matrix, $\mathbf{\Psi}_0 = \text{1e-2}\mathbf{I}_{3\times3}$. The adaptation is initialized with this same random value. The adaptation buffer is set to be $m_b = 30$ and the adaptation process noise and measurement noise are set to be $\mathbf{Q}_w = \text{1e-7}\mathbf{I}_{3\times3}$ and $\mathbf{R}_w = \text{1e-2}\mathbf{I}$ respectively. Since there are no unmodeled perturbations on the chaser vehicle, there is no process noise applied to the chaser vehicle dynamics in the filter. The discrete time process noise matrix for the chaser accelerometer bias is set to be $\text{3.433e-8}\mathbf{I}m/s^2$.

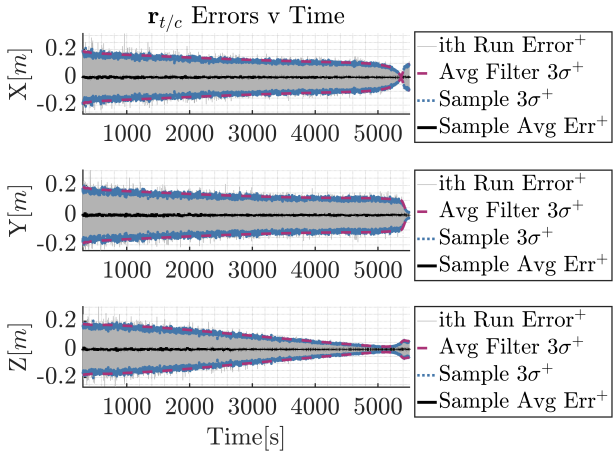

Fig. 8 Relative position of the target vehicle errors in the target RTN frame versus time excluding initial 300s.

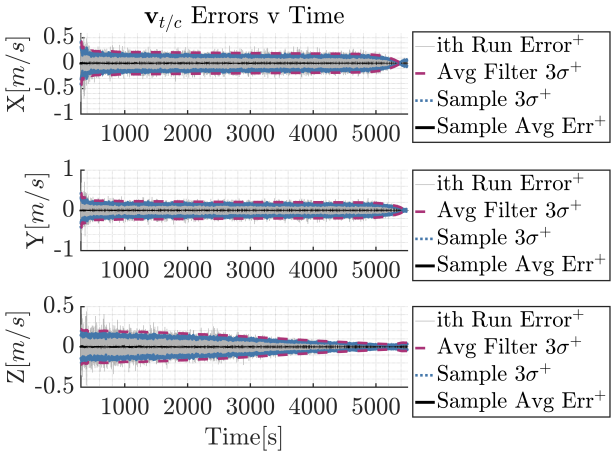

Fig. 9 Relative velocity of the target vehicle errors in the target RTN frame versus time excluding initial 300s.

It is clear that the adaptation successfully compensates for the unknown, regular venting by examining the average $3\sigma^+$ intervals compared with the sample $3\sigma^+$ intervals in Figures 8–10. Similar to the results of the pervious scenario, while the estimated intervals in Figures 9 and 10 overestimate the errors in the relative velocity and acceleration, the intervals for the relative position nearly overlay the sample estimates.

In this scenario the estimated and sample uncertainty intervals match more closely for the relative velocity and the unmodeled target acceleration. For additional analysis, the prior measurement residuals and their 3σ intervals are shown in Figures 12 and 13. The sample and the estimated $3\sigma^-$ intervals match well. Finally, Figure 11 is included to demonstrate that employing a dual usage accelerometer strategy in cislunar space functions just as well as in a gravity well.

The results for the NRHO scenario, presented in Figures 8-13, show for this scenario are similar to that of the pervious scenario. Differences in the scale are largely due to the slight differences in the relative distance between the two spacecraft and differences in the condition number of the observability Gramian from one scenario to the next. There is less relative motion between the two spacecraft in the NRHO scenario than in the Earth centered scenario, which can cause more difficult numeric conditioning for the observability Gramian for the NRHO scenario. The results presented here demonstrate that the MILTON algorithm is capable of providing well suited process noise covariance intervals for spacecraft operating in a strong gravity well as well as in cislunar space.

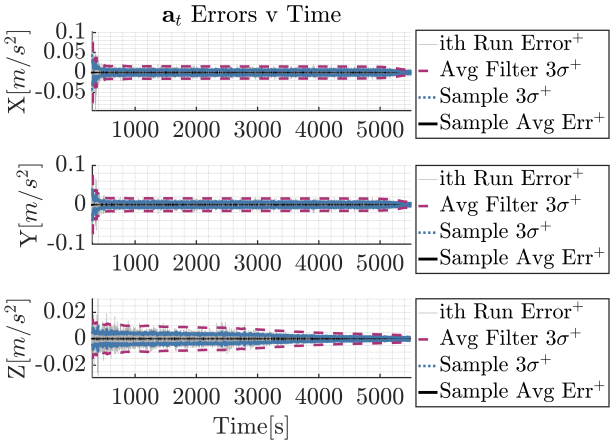

Fig. 10 Unmodeled acceleration of the target vehicle errors in the target RTN frame versus time excluding initial 300s.

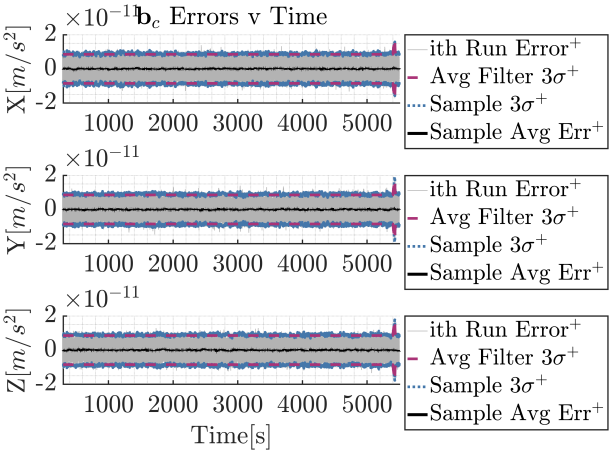

Fig. 11 Chaser accelerometer bias errors in the chaser body frame versus time excluding initial 300s.

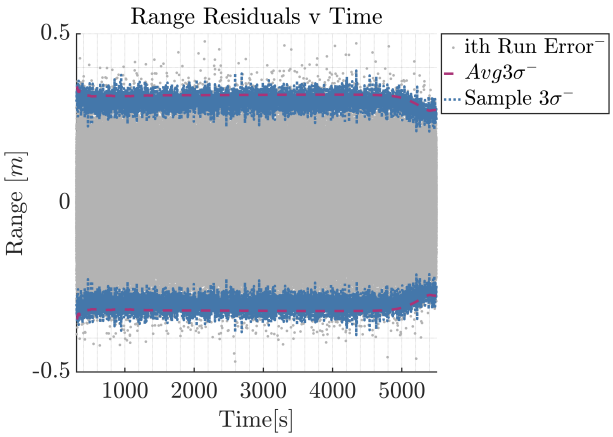

Fig. 12 Range measurement residuals versus time excluding initial 300s.

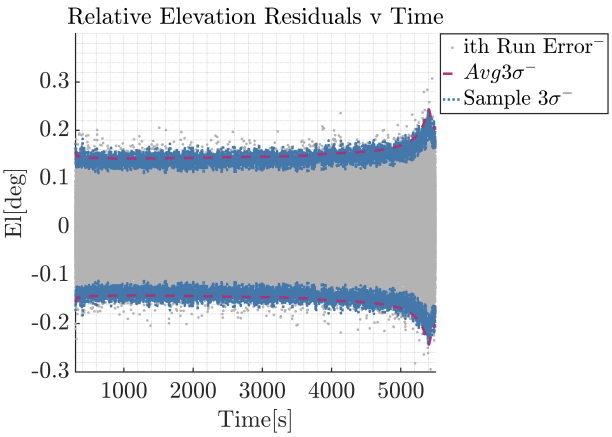

Fig. 13 Elevation measurement residuals versus time excluding initial 300s.

V. Conclusions

The ability to adapt to changing conditions is vital to the future of space exploration. As humans venture forth on missions to distant celestial bodies there is a greater necessity for robust solutions to keep the crews safe. While there has been extensive research into venting disturbances caused by the presence of a crew, there is no guarantee that the system will behave as modeled. Off nominal behavior can be induced by a variety of factors and may be influenced by factors that no one has considered. Venting is the subject of this study, but there are countless sources of model mismatch for space vehicles. For this reason, adaptive methods are a clear need to ensure the success of future space missions.

This work demonstrates that correlation methods can be effectively utilized to enable a filter to autonomously adapt to unknown venting disturbances within a nonlinear, onboard, relative navigation scenario. Unlike prior studies where correlation methods were applied to linear systems, this research extends their application to environments with both minor and major unmodeled perturbations to a nonlinear system. The algorithm, referred to as MILTON, successfully recovers and maintains a well-contained solution under these conditions. Historically, the positive definiteness of process noise in such studies has often been addressed heuristically. Other research has preserved definiteness using Riemann manifolds, albeit with significant computational expenses. In contrast, this work ensures positive definiteness is maintained efficiently by utilizing the kinematic relationship between position, velocity, and acceleration. Finally, the information form of recursive least squares is utilized to mitigate the computational demands of the adaptation block.

This study shows that correlation methods can be successfully applied to both bounded planetary orbits as well as cislunar orbits. Additionally, this study shows that correlation methods can be used to estimate uncertainty contributions from time correlated uncertainty in spacecraft dynamics as well as more random perturbations like vehicle vents. In future work, unmodeled target vehicle maneuvers will be examined and MILTON will be adjusted to accommodate larger model discrepancies.

Funding Sources

This work was supported by a NASA Space Technology Graduate Research Opportunity, NASA grant number: 80NSSC22K1204.

References

[1] D'Souza, C., and Zanetti, R., "Navigation Design and Analysis for the Orion Earth-Moon Mission," *AAS/AIAA Space Flight Mechanics Conference*, 2014.

[2] D'Souza, C. D., and Zanetti, R., "A First Look at the Navigation Design and Analysis for the Orion Exploration Mission 2," *AAS/AIAA Astrodynamics Specialist Conference 2017*, 2017.

[3] Joshi, J. A., and D'Souza, C. N., "Modeling Venting Disturbances Within Linear Covariance Toolset for Crewed Artemis Missions," *AAS/AIAA Astrodynamics Specialist Conference*, 2023.

[4] Joshi, J. A., Gualdoni, M. J., D'Souza, C. N., Woffinden, D. C., McCabe, J. S., and York, C., "Artemis II: Linear Covariance Analysis Using Explicit Vent Force States," *AAS/AIAA Astrodynamics Specialist Conference*, 2024.

[5] Kalman, R. E., "A New Approach to Linear Filtering and Prediction Problems," *Transactions of the ASME, Journal of Basic Engineering*, Vol. 82, No. 1, 1960, pp. 35–45. https://doi.org/10.1115/1.3662552.

[6] Kalman, R. E., and Bucy, R. S., "New Results in Linear Filtering and Prediction Theory," *Transactions of the ASME, Journal of Basic Engineering*, Vol. 83, No. 1, 1961, pp. 95–108. https://doi.org/10.1115/1.3658902.

[7] Mehra, R., "On the Identification of Variances and Adaptive Kalman Filtering," *IEEE Transactions on Automatic Control*, Vol. 15, No. 2, 1970, pp. 175–184. https://doi.org/10.1109/TAC.1970.1099422.

[8] Mehra, R., "Approaches to Adaptive Filtering," *IEEE Transactions on Automatic Control*, Vol. 17, No. 5, 1972, pp. 693–698. https://doi.org/10.1109/TAC.1972.1100100.

[9] Bélanger, P. R., "Estimation of Noise Covariance Matrices for a Linear Time-Varying Stochastic Process," *Automatica*, Vol. 10, No. 3, 1974, pp. 267–275. https://doi.org/10.1016/0005-1098(74)90037-5, URL https://www.sciencedirect.com/science/article/pii/0005109874900375.

[10] Duník, J., Straka, O., and Šimandl, M., "On Autocovariance Least-Squares Method for Noise Covariance Matrices Estimation," *IEEE Transactions on Automatic Control*, Vol. 62, No. 2, 2017, pp. 967–972. https://doi.org/10.1109/TAC.2016.2571899.

[11] Odelson, B. J., Rajamani, M. R., and Rawlings, J. B., "A New Autocovariance Least–Squares Method for Estimating Noise Covariances," *Automatica*, Vol. 42, No. 2, 2006, pp. 303–308. https://doi.org/https://doi.org/10.1016/j.automatica.2005.09.006, URL https://www.sciencedirect.com/science/article/pii/S0005109805003262.

[12] Åkesson, B. M., Jørgensen, J. B., Poulsen, N. K., and Jørgensen, S. B., "A Generalized Autocovariance Least–Squares Method for Kalman Filter Tuning," *Journal of Process Control*, Vol. 18, No. 7, 2008, pp. 769–779. https://doi.org/https://doi.org/10.1016/j.jprocont.2007.11.003, URL https://www.sciencedirect.com/science/article/pii/S0959152407001631.

[13] Duník, J., Kost, O., and Straka, O., "Design of Measurement Difference Autocovariance Method for Estimation of Process and Measurement Noise Covariances," *Automatica*, Vol. 90, 2018, pp. 16–24. https://doi.org/https://doi.org/10.1016/j.automatica.2017.12.040, URL https://www.sciencedirect.com/science/article/pii/S0005109817306271.

[14] Moghe, R., Zanetti, R., and Akella, M. R., "Adaptive Kalman Filter for Detectable Linear Time-Invariant Systems," *Journal of Guidance, Control, and Dynamics*, Vol. 42, No. 10, 2019, pp. 2197–2205. https://doi.org/10.2514/1.G004359, URL https://doi.org/10.2514/1.G004359.

[15] Moghe, R., "Adaptive Algorithms for Identification of Symmetric and Positive Definite Matrices," Ph.D. thesis, The University of Texas at Austin, 2021.

[16] Sage, A. P., and Husa, G. W., "Adaptive Filtering with Unknown Prior Statistics," *Proceedings of the Joint Automatic Control Conference*, 1969, pp. 760–769.

[17] Myers, K., and Tapley, B., "Adaptive Sequential Estimation with Unknown Noise Statistics," *IEEE Transactions on Automatic Control*, Vol. 21, No. 4, 1976, pp. 520–523. https://doi.org/10.1109/TAC.1976.1101260.

[18] Rajamani, M. R., and Rawlings, J. B., "Estimation of the Disturbance Structure from Data Using Semidefinite Programming and Optimal Weighting," *Automatica*, Vol. 45, No. 1, 2009, pp. 142–148. https://doi.org/https://doi.org/10.1016/j.automatica.2008.05.032, URL https://www.sciencedirect.com/science/article/pii/S000510980800366X.

[19] Stacey, N., and D'Amico, S., "Adaptive and Dynamically Constrained Process Noise Estimation for Orbit Determination," *IEEE Transactions on Aerospace and Electronic Systems*, Vol. 57, No. 5, 2021, pp. 2920–2937. https://doi.org/10.1109/TAES.2021.3074205.

[20] Moghe, R., Zanetti, R., and Akella, M., "Covariance Matching Kalman Filter for Observable LTI Systems," *2018 IEEE Conference on Decision and Control (CDC)*, 2018, pp. 6372–6377. https://doi.org/10.1109/CDC.2018.8619203.

[21] Shumway, R. H., and Stoffer, D. S., "An Approach to Time Series Smoothing and Forecasting Using the EM Algorithm," *Journal of Time Series Analysis*, Vol. 3, No. 4, 1982, pp. 253–264. https://doi.org/10.1111/j.1467-9892.1982.tb00349.x.

[22] Axelsson, P., Orguner, U., Gustafsson, F., and Norrlöf, M., "ML Estimation of Process Noise Variance in Dynamic Systems," *IFAC Proceedings Volumes*, Vol. 44, No. 1, 2011, pp. 5609–5614. https://doi.org/https://doi.org/10.3182/20110828-6-IT-1002.00543, URL https://www.sciencedirect.com/science/article/pii/S1474667016445003, 18th IFAC World Congress.

[23] Kashyap, R., "Maximum Likelihood Identification of Stochastic Linear Systems," *IEEE Transactions on Automatic Control*, Vol. 15, No. 1, 1970, pp. 25–34. https://doi.org/10.1109/TAC.1970.1099344.

[24] Lainiotis, D., "Optimal Adaptive Estimation: Structure and Parameter Adaption," *IEEE Transactions on Automatic Control*, Vol. 16, No. 2, 1971, pp. 160–170. https://doi.org/10.1109/TAC.1971.1099684.

[25] Magnant, C., Giremus, A., Grivel, E., Ratton, L., and Joseph, B., "Bayesian Non–Parametric Methods for Dynamic State–Noise Covariance Matrix Estimation: Application to Target Tracking," *Signal Processing*, Vol. 127, 2016, pp. 135–150. https://doi.org/https://doi.org/10.1016/j.sigpro.2016.02.013, URL https://www.sciencedirect.com/science/article/pii/S0165168416000633.

[26] Huang, Y., Zhang, Y., Wu, Z., Li, N., and Chambers, J., "A Novel Adaptive Kalman Filter with Inaccurate Process and Measurement Noise Covariance Matrices," *IEEE Transactions on Automatic Control*, Vol. 63, No. 2, 2017, pp. 594–601. https://doi.org/10.1109/TAC.2017.2730480.

[27] Mussot, V., Mercère, G., Dairay, T., Arvis, V., and Vayssettes, J., "Noise Covariance Matrix Estimation with Subspace Model Identification for Kalman Filtering," *International Journal of Adaptive Control and Signal Processing*, 2021. https://doi.org/10.1002/acs.3213.

[28] Simpkins, A., "System Identification: Theory for the User, 2nd Edition (Ljung, L.; 1999) [On the Shelf]," *IEEE Robotics Automation Magazine*, Vol. 19, No. 2, 2012, pp. 95–96. https://doi.org/10.1109/MRA.2012.2192817.

[29] Schutz, B., Tapley, B., and Born, G. H., *Statistical Orbit Determination*, Elsevier, 2004.

[30] Stauch, J., and Jah, M., "Unscented Schmidt–Kalman Filter Algorithm," *Journal of Guidance, Control, and Dynamics*, Vol. 38, No. 1, 2015, pp. 117–123. https://doi.org/10.2514/1.G000467.

[31] McCabe, J. S., and DeMars, K. J., "Square–Root Consider Filters with Hyperbolic Householder Reflections," *Journal of Guidance, Control, and Dynamics*, Vol. 41, No. 10, 2018, pp. 2098–2111. https://doi.org/10.2514/1.G003417.

[32] Zanetti, R., Holt, G., Gay, R., D'Souza, C., Sud, J., Mamich, H., Begley, M., King, E., and Clark, F. D., "Absolute Navigation Performance of the Orion Exploration Flight Test 1," *Journal of Guidance, Control, and Dynamics*, Vol. 40, No. 5, 2017, pp. 1106–1116. https://doi.org/10.2514/1.G002371.

[33] Roth, D., Hahn, Y., Owen, B., and Wagner, S. V., "Cassini In-Flight Navigation Adaptations," *2018 SpaceOps Conference*, 2018, p. 2647.

[34] Gramling, C., Lorah, J., Santoro, E., Work, K., Chambers, R., and Bauer, F. H., "Preliminary Operational Results of the TDRSS Onboard Navigation System (TONS) for the Terra Mission," *Spaceflight Dynamics*, 2000.

[35] Giraldo-Grueso, F., Popov, A. A., and Zanetti, R., "Precision Mars Entry Navigation with Atmospheric Density Adaptation Via Neural Networks," *Journal of Aerospace Information Systems*, 2024, pp. 1–14. https://doi.org/10.2514/1.I011426.

[36] Giraldo-Grueso, F., Popov, A. A., and Zanetti, R., "Adaptive Mart Entry Guidance with Atmospheric Density Estimation," *Proceedings of the AAS/AIAA Astrodynamics Specialist Conference, Broomfield, Colorado*, 2024.

[37] Zanetti, R., and D'Souza, C., "Dual Accelerometer Usage Strategy for Onboard Space Navigation," *Journal of Guidance, Control, and Dynamics*, Vol. 35, No. 6, 2012, pp. 1899–1902. https://doi.org/10.2514/1.58154.

[38] Duník, J., Straka, O., Kost, O., and Havlík, J., "Noise Covariance Matrices in State-Space Models: A Survey and Comparison of Estimation Methods-Part I," *International Journal of Adaptive Control and Signal Processing*, Vol. 31, No. 11, 2017, pp. 1505–1543. https://doi.org/10.1002/acs.2783.

[39] Singer, R. A., "Estimating Optimal Tracking Filter Performance for Manned Maneuvering Targets," *IEEE Transactions on Aerospace and Electronic Systems*, Vol. AES-6, No. 4, 1970, pp. 473–483. https://doi.org/10.1109/TAES.1970.310128.

[40] Zanetti, R., "Adaptable Recursive Update Filter," *Journal of Guidance, Control, and Dynamics*, Vol. 38, No. 7, 2015, pp. 1295–1300. https://doi.org/10.2514/1.G001031.

[41] Servadio, S., Zanetti, R., and Jones, B. A., "Nonlinear Filtering with a Polynomial Series of Gaussian Random Variables," *IEEE Transactions on Aerospace and Electronic Systems*, Vol. 57, No. 1, 2020, pp. 647–658. https://doi.org/10.1109/TAES.2020.3028487.

[42] McGuire, M. L., McCarty, S. L., and Burke, L. M., "Power and Propulsion Element (PPE) Spacecraft Reference Trajectory Document," Tech. rep., 2020.

[43] Newman, C. P., Davis, D. C., Whitley, R. J., Guinn, J. R., and Ryne, M. S., "Stationkeeping, Orbit Determination, and Attitude Control for Spacecraft in Near Rectilinear Halo Orbits," *AAS Astrodynamics Specialists Conference*, 2018.

[44] Davis, D., Bhatt, S., Howell, K., Jang, J.-W., Whitley, R., Clark, F., Guzzetti, D., Zimovan, E., and Barton, G., "Orbit Maintenance and Navigation of Human Spacecraft at Cislunar Near Rectilinear Halo Orbits," *AAS/AIAA Space Flight Mechanics Meeting*, 2017.

[45] Amzajerdian, F., Pierrottet, D., Petway, L. B., Hines, G. D., Roback, V. E., and Reisse, R. A., "Lidar Sensors for Autonomous Landing and Hazard Avoidance," *AIAA SPACE 2013 Conference and Exposition*, 2013, p. 5312.

[46] Setterfield, T. P., Hewitt, R. A., Chen, P.-T., Espinoza, A. T., Trawny, N., and Katake, A., "Lidar-Inertial Based Navigation and Mapping for Precision Landing," *2021 IEEE Aerospace Conference (50100)*, IEEE, 2021, pp. 1–19.

[47] Vallado, D. A., *Fundamentals of Astrodynamics and Applications*, Vol. 12, Springer Science & Business Media, 2001.